

Dark current investigation of a direct-current and superconducting radio-frequency combined photocathode gun*

Tianyi Li,¹ Haoyan Jia,¹ Juntao Liu,¹ Lin Lin,¹ Fei Jiao,¹ Liwen Feng,¹ Shengwen Quan,¹ Jingyi Li,² and Senlin Huang^{1,†}

¹State Key Laboratory of Nuclear Physics and Technology and Institute of Heavy Ion Physics,
School of Physics, Peking University, Beijing 100871, China

²Institute of High Energy Physics, Chinese Academy of Sciences, Beijing 100049, China

Photocathode guns with a low dark current are highly desired, especially in the case of high-brightness continuous-wave (CW) operation. The direct current - superconducting radiofrequency (DC-SRF) gun, a hybrid photocathode gun combining a direct-current gap and a superconducting radiofrequency (SRF) cavity, effectively isolates the photocathode from the SRF cavity and offers significant advantages in minimizing dark current levels. This paper presents an in-depth study on the dark current of the newly developed high-brightness DC-SRF photocathode gun (DC-SRF-II gun). Especially, a systematic experimental investigation of the dark current has been conducted and a comprehensive understanding of its formation has been achieved through compliant simulation and measurement. Besides, measures for attaining sub-nanoampere dark current in the DC-SRF-II gun are presented, including design considerations, cavity processing, assembly, and conditioning. Our work establishes a strong foundation for achieving high-performance operation of the DC-SRF-II gun and also provides valuable reference for other photocathode guns.

Keywords: Dark current, Photocathode gun, DC conditioning, RF conditioning, Tracking simulation

I. INTRODUCTION

High-brightness photocathode electron guns play an important role in various applications such as free-electron lasers (FELs) [1–6], energy recovery linacs (ERLs) [7–9], and ultrafast electron diffraction (UED) [10–12]. As one of the major limitations for high-brightness operation, the dark current from the gun, originating from the field emission on the inner walls of its accelerating structure, has been attracting considerable attention [13–33]. Such a current is undesirable from the perspective of stable operation. Particularly, for those accelerators operated in continuous-wave (CW) mode, a large amount of dark current may limit the overall performance and the long-term reliability of the accelerators [15].

DC guns, VHF guns, and SRF guns are the primary types of electron guns designed for continuous-wave free-electron laser (CW FEL) applications, which require high-repetition-rate operation. Table I summarizes some typical guns for CW applications. DC electron guns exhibit remarkable performance in GHz repetition rate operation with extremely low dark current. The cathode surface field, reaching several MV/m, allows DC high-voltage electron guns to achieve exceptionally low dark current, typically in the picoampere (pA) range [19, 21]. For instance, JAEA reported an accurate measurement of just 50 pA for the dark current in their DC gun [25]. Normal-conducting (NC) very high frequency (VHF) electron guns operate effectively in the MHz continuous-wave regime, producing high-brightness beams. Research on VHF guns is actively conducted at institutions such as LBNL, SLAC [27, 30], Tsinghua University [32],

the Shanghai High Repetition Rate XFEL and Extreme Light Facility (SHINE), and the Shanghai Advanced Research Institute (SARI) [33]. At SLAC, the dark current of the VHF gun was successfully reduced to 2.6 μ A at a distance of 1.5 meters using a collimator. At ZJLAB and SARI, dark current suppression was achieved by employing a precisely over-inserted plug, which decreased both the electric field intensity and the dark current transmission ratio. Experiments with the ZJLAB/SARI VHF gun demonstrated substantial reduction, lowering the dark current to the level of field current noise (~ 1 nA) using a 0.3–0.6 mm over-inserted plug at 870 kV. Additionally, implementing a 0.5 mm over-inserted plug in the SHINE VHF gun significantly reduced the dark current from 570 nA to just 2 nA at 810 kV. SRF electron guns can operate at higher energy with low dark currents. The SRF gun-II developed at HZDR, which uses a 3.5-cell TESLA-type cavity as its accelerating unit, has been reported to generate a 3.5 MeV beam with dark currents on the order of 100 nA [31]. The QWR electron gun at BNL can generate 1–1.5 MeV electron beam and the dark current was at picoampere (pA) level [26]. Although the dark current might be reduced via collimators or fast kickers [20, 22, 33], photocathode guns with a low dark current are highly desired, especially in the case of high-brightness CW operation.

The DC-SRF gun, a direct-current (DC) and superconducting radio-frequency (SRF) combined photocathode electron gun developed at Peking University [34–39], is expected to operate in CW mode with a dark current below 1 nanoampere (nA). It can generate electron beams with a repetition rate of 1 MHz and above, an average current up to a few milliamperes (mA), and an energy of a few megavolts (MeV). Its photocathode is located in the DC gap and therefore separated from the SRF cavity. This can not only avoid the contamination of the cavity from the semiconductor materials, but also greatly diminish the dark current arising from the insertion of the photocathode plug into the cathode nose of an electron gun. The development of the DC-SRF gun has

* Supported by the National Key Research and Development Program of China (Grant No. 2016YFA0401904 and 2017YFA0701001) and the State Key Laboratory of Nuclear Physics and Technology, Peking University (Grant No. NPT2022ZZ01).

† Corresponding author, Senlin Huang, huangsl@pku.edu.cn.

TABLE 1. Summary of CW guns' parameters

Parameters	Gun energy	Gradient on photocathode	Demonstrated emittance	Dark current
Cornell DC gun	0.4 MeV	4.4 MV/m	$\sim 0.4 \mu\text{m}$ @ 100 pC	pA level
JAEA DC gun	0.5 MeV	5.8 MV/m	$0.45 \mu\text{m}$ @ 100 pC	50 pA
SLAC VHF gun	0.65 MeV	17.5 MV/m	$\sim 0.5 \mu\text{m}$ @ 50 pC	μA level
THU VHF gun	0.78 MeV	27 MV/m	0.429 @ 50 pC; 0.853 @ 100 pC	2 nA (SHINE)
ZJLAB/SARI VHF gun	0.87 MeV	19.8 MV/m	N/A	1 nA
BNL SRF gun	1-1.5 MeV	18 MV/m	$\sim 0.3 \mu\text{m}$ @ 100 pC	pA level
HZDR SRF gun-II	3.5 MeV	14 MV/m	$2 \mu\text{m}$ @ 200 pC	100 nA
PKU DC-SRF gun	1.8-2.4 MeV	6 MV/m	0.4 @ 50 pC; 0.54 @ 100 pC	2.8-177 pA

undergone three stages: the prototype (DC-SC), the first generation (DC-SRF-I), and the second generation (DC-SRF-II). The DC-SRF-II gun is operated at the DC voltage of 100 kV and an SRF cavity gradient of about 14 MV/m. It employs K_2CsSb photocathode and the 515 nm drive laser has a longitudinally quasi-plateau distribution with a length of 20-30 ps. Simulation studies show the bunch length is at 10 ps level. The gun has achieved stable CW operation recently [39], delivering a few MeV electron beam at 1 MHz and 81.25 MHz repetition rates, with an average current up to 3 mA and the dark current several orders lower than current normal conducting CW guns. In this paper, we present a comprehensive investigation on the dark current of the DC-SRF-II gun from both the simulation and experiment aspects. Our study provides an efficient method for dark current analysis, which accurately reveals the formation of the dark current in the DC-SRF gun. This lays a solid foundation for improving the performance of the gun. The remaining part is organized as follows. Sec. II provides a brief description of the DC and SRF hybrid structure, along with the electric field distribution inside. Sec. III presents the experimental results, covering the conditioning of the DC electrodes and the SRF cavity, as well as the dark current measurement results. Sec. IV presents the analysis and discussion based on field-emitted electron tracking and experimental data fitting. Finally, we give a brief summary in Sec. V.

II. DC-SRF HYBRID STRUCTURE AND ELECTRIC FIELD DISTRIBUTION

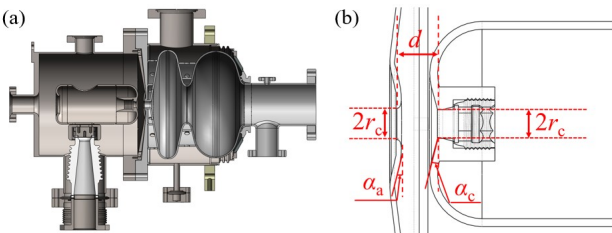


Fig. 1. The DC-SRF hybrid structure for the DC-SRF-II gun. (a) Assembly diagram of the SRF cavity and the DC gap. (b) A detailed view of the anode and cathode surfaces with key dimensions labeled.

The acceleration structure of the DC-SRF-II gun is shown in Fig. 1(a), which comprises a pair of DC high voltage electrodes, referred to as the “DC gap” hereon, and a 1.3 GHz 1.5-cell SRF cavity connected by a short drift tube with a length of 11 mm. The DC gap adopts a cathode column-anode plate design whose geometry is characterized by the parameters illustrated in Fig. 1(b). The cathode side has a hole with a radius of $r_c = 5.5$ mm, where the photocathode plug is located, while the anode side has a hole with a radius of $r_a = 6$ mm, which allows for a no-loss transport of the electron beam. The distance between the two holes (d) is 15.5 mm, over which a voltage of 100 kV is exerted. Around the holes, the cathode surface has an inclination angle of $\alpha_c = 15^\circ$ and the anode surface has an inclination angle of $\alpha_a = 19.7^\circ$, which provide the required electric force to focus the electron beam. To achieve a lower ratio between the surface fields of the electrodes and photocathode, the cathode column has a round corner with a radius of 20 mm and the anode hole has an elliptical chamfer where the major and minor axes for the ellipse are 26.8 mm and 5.0 mm, respectively.

The electric field distribution of the DC gap is shown in Fig. 2(a), where the maximum gradient has been restricted within 10 MV/m to reduce the risk of discharging when operating the gun with a DC voltage of 100 kV. Special attention has been paid to the cathode plug area, for which the electric field is plotted in Fig. 2(b). One can see that the field gradient is 6 MV/m within the central region of the cathode plug. Peaks at the edges of the cathode plug can also be observed; however, they would not cause problems since the field (less than 6.7 MV/m) is still within a relatively safe range.

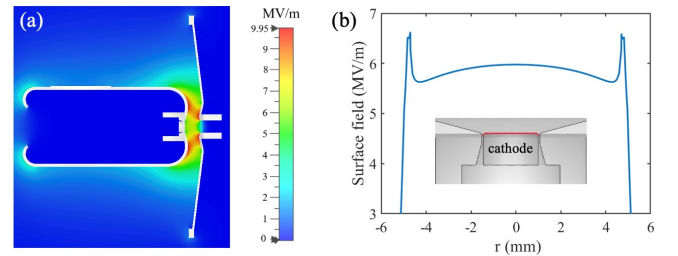


Fig. 2. Simulated electric field of the DC gap at a DC voltage of 100 kV. (a) Two-dimensional electric field distribution in the gap region. (b) Electric field at the cathode plug surface (along the path indicated by the red line in the inset).

The SRF cavity comprises a specially designed half cell and a TESLA-type full cell, which would accelerate the 100 keV electron beam from the DC gap to about 2 MeV. The half cell has a conical back wall with an inclination angle of 10.5° and an entrance iris with a radius of 6 mm, which is connected to the DC gap with the short drift tube, as shown in Fig. 3(a). When the SRF cavity is operated with an accelerating gradient (E_{acc}) of 17.4 MV/m, corresponding to an on-axis peak electric field ($E_{z,\text{max}}$) of 27 MV/m, the maximum electric field on the cavity surface is 32.1 MV/m, which occurs around the entrance iris of the full cell, while the electric field around the entrance iris of the half cell has a local maximum of 24.7 MV/m, as shown in Fig. 3(b). Therefore, field emission is more likely to happen near these cavity irises.

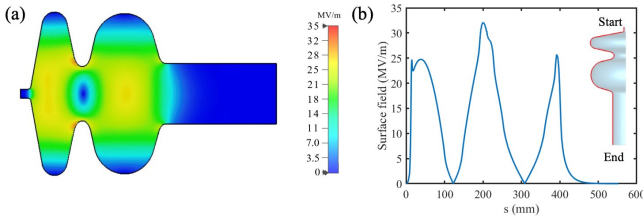


Fig. 3. Simulated electric field of the SRF cavity at an E_{acc} of 17.4 MV/m (corresponding to an $E_{z,\text{max}}$ of 27 MV/m). (a) Electric field distribution in the SRF cavity. (b) Surface electric field of the SRF cavity (along the path indicated by the red line in the inset).

The cathode column, made of 316 L stainless steel, is mounted on a conical reverse ceramic, while the anode plate, made of pure titanium, is detachable from the SRF cavity. Such a design allows independent polishing and cleaning of the electrodes, thereby helping to improve the operation voltage. The SRF cavity is manufactured from large grain niobium plate and undergoes a series of post-treatments, including buffered chemical polishing (BCP), high-pressure rinsing (HPR), and high-temperature annealing. The assembly of the DC electrodes and SRF cavity was performed in a Class-100 clean room to reduce contamination from dust particles.

III. EXPERIMENTS

A. DC electrodes conditioning

The DC components were first conditioned to eliminate the field emission at the expected operation voltage of 100 kV, for which the DC-SRF hybrid structure was vacuumized to about 1×10^{-5} Pa, while the cryostat was vacuumized to about 1×10^{-4} Pa. In order to avoid high-voltage discharge-induced damage, all the vacuum gauges were turned off during the conditioning, and the ion pump current readouts were used instead as a measurement of the vacuum. The ion current of the pump for the SRF cavity therefore served as a monitoring signal for arcing (vacuum breakdown) events between the cathode and the anode.

Fig. 4(a) shows the recorded DC voltage and vacuum signal during the conditioning. The voltage was ramped to 70 kV in

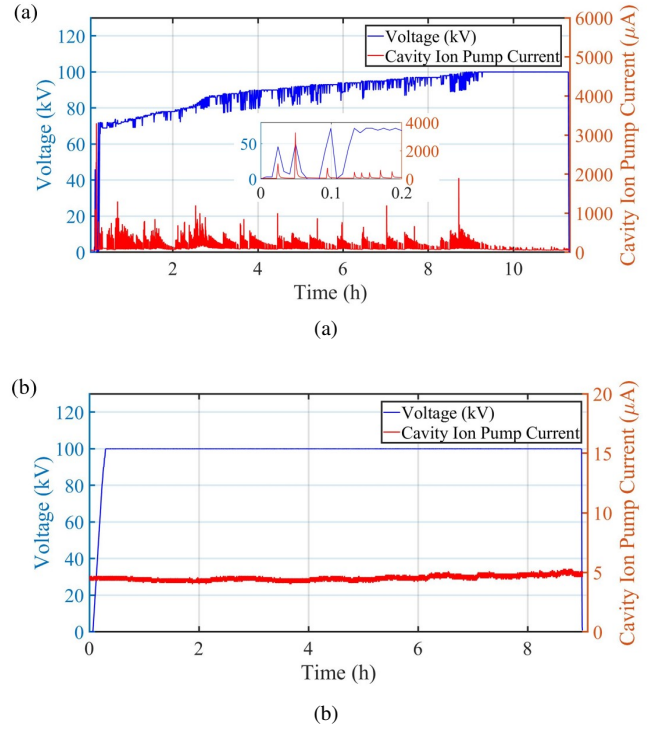


Fig. 4. DC voltage and vacuum signals during the conditioning (a) and the 100 kV operation test (b). The inset in (a) is a local enlarged plot for the first 12 minutes. The conditioning was performed at room temperature, while the operation test was performed when the DC-SRF-II gun was cooled down.

less than 10 minutes. During this initial stage, the interlock protection was triggered by the arcing signal from the DC gap only a few times. The voltage ramping was slowed down above 72 kV, when the arcing started to occur frequently. It took about 160 minutes to reach a voltage of 86 kV. During this second stage, the voltage was only decreased by a few kV when the interlock protection was triggered, since no significant temperature rise was observed from the temperature probes attached to the vacuum chamber of the DC components.

In the third stage, the voltage was ramped from 86 kV to 100 kV in more than 6 hours. The ramping step was set to 1 kV, and the maximum voltage decrement for interlock protection was increased to 10 kV. Finally, the voltage was maintained at 100 kV for about 2 hours with the ion current stabilized at the background level. It is worth noting that no arcing was observed at the junctions of high-voltage cables in the cryostat during the entire conditioning process.

A nine-hour operation test was carried out after the DC-SRF-II gun was cooled down. As illustrated in Fig. 4(b), the DC voltage was very stable and the vacuum signal was at the background level. This indicates that the conditioning has effectively reduced the number of field emitters in the DC gap, which is a crucial step for achieving low dark current operation in the DC-SRF gun.

B. SRF cavity conditioning

RF conditioning was performed after cooling down the SRF cavity. For hardware safety considerations, the SRF cavity was operated in pulsed mode with a duty cycle of 10%. During the conditioning, the DC voltage was set to zero, and only the dark current from the SRF cavity was monitored. The beam line for RF conditioning and dark current study is sketched in Fig. 5, which mainly includes a solenoid lens, a Faraday cup (FC), and an yttrium aluminum garnet (YAG) screen. The solenoid, FC, and YAG screen are located 1.0 m, 1.3 m, and 1.5 m downstream from the photocathode, respectively. The field-emitted electrons are focused by the solenoid and collected by the FC. The FC signal, representing the dark current, is recorded by a picoammeter with a resolution of 0.1 picoampere (pA). Meanwhile, the YAG screen, together with a 45° reflection mirror and a CCD camera, is used to image the electrons.

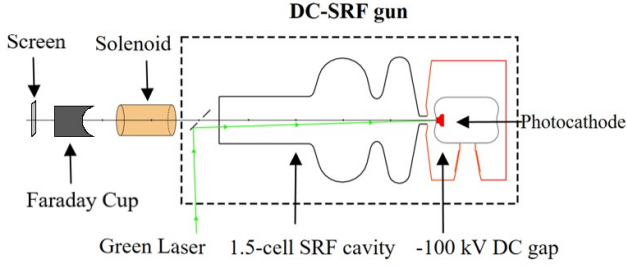


Fig. 5. A schematic view of the gun and the dark current diagnostics.

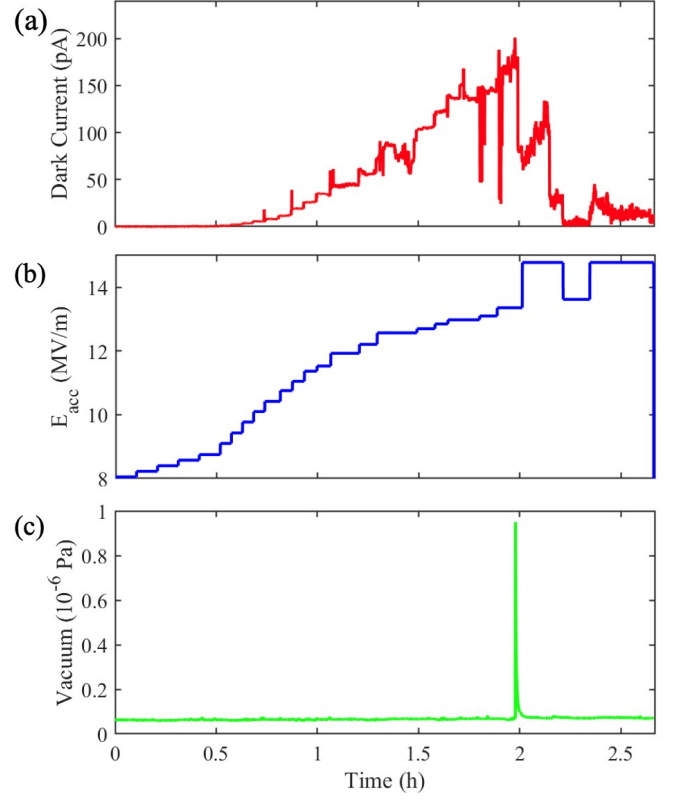


Fig. 6. Dark current and cavity vacuum through the RF conditioning process of the SRF cavity. (a) and (c) display the monitored dark current and cavity vacuum, respectively. (b) illustrates the adjustment of the SRF cavity gradient during the RF conditioning.

Figure 6 illustrates the monitoring results of dark current and cavity vacuum through the RF conditioning process. Upon raising the accelerating gradient to 9.1 MV/m, a weak dark current of 1 pA was initially detected, and a subtle image could be observed on the YAG screen. As the gradient continued to increase, the dark current overall exhibited a stepwise growth and reached a maximum of 201 pA at a gradient of 13.4 MV/m. Then, a fluctuation in the cavity's vacuum was observed for the first time, increasing from 6.7×10^{-8} Pa to 9.5×10^{-7} Pa. The vacuum then quickly returned to the initial level, and the dark current simultaneously underwent a rapid decline, reaching a value of 63 pA. This indicates an enhancement of the cavity surface condition attributed to significant field emission.

Afterwards, the cavity gradient was raised to 14.8 MV/m, 10% higher than the desired value for nominal operations of the DC-SRF-II gun. The dark current gradually increased to 134 pA and then underwent a rapid decline to the level of 30 pA. Subsequently, we decreased the cavity gradient to 13.6 MV/m, and the dark current fell to a few pA. Finally, the gradient was set back to 14.8 MV/m, where the dark current eventually remained at a lower level with an average value around 14 pA.

C. Dark current measurements

Measurements were conducted to separately evaluate the dark current originating from the DC gap and the SRF cavity. To measure the dark current originating from the DC gap accurately, the SRF cavity was operated in CW mode with a lower accelerating gradient close to 10 MV/m, where it did not generate detectable dark current. The DC voltage was set at 100 kV, and the solenoid field was scanned over a wide range. The picoammeter readout consistently remained at zero throughout the scanning process, indicating that the dark current from the DC gap was less than 0.1 pA and could be neglected in the experiments.

To measure the dark current originating from the SRF cavity, the RF was switched to pulse mode with a 10% duty cycle to ensure RF system safety. **The accelerating gradient of the cavity was scanned between 10 MV/m and 14.8 MV/m. At each step, the solenoid field was initially scanned to maximize the picoammeter readout, after which 90 data points were collected and the average was recorded as the result.**

A dark current of 0.28 pA was first detected at the accelerating gradient of 11.1 MV/m. As the gradient increased, the dark current showed an exponential growth trend, reaching a maximum of 17.7 pA at 14.8 MV/m (see the blue plots in Fig. 7). This corresponds to a dark current of 177 pA for

254 CW operation, taking into consideration a linear dependency
255 of the dark current on the RF duty factor.

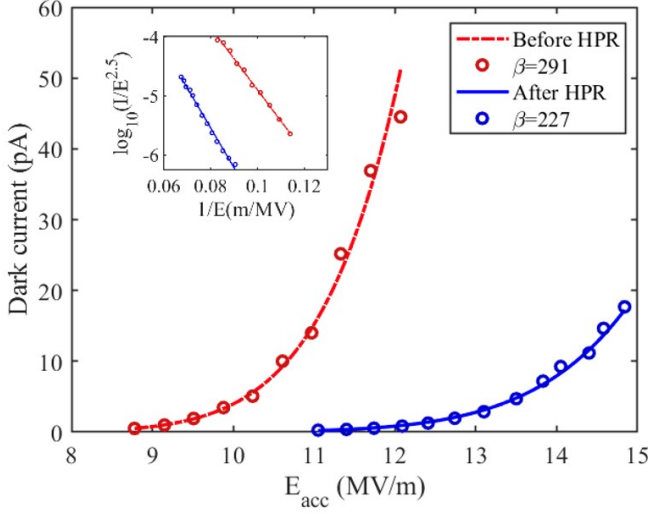


Fig. 7. Dark current measurement and fitting results of the DC-SRF-II gun. The red plots are the results from an early-stage operation, while the blue plots are the results during the latest operation after SRF cavity high-pressure rinsing (HPR) and reassembly. The circles depict the experimental data, while the lines represent the fitting curves based on the F-N theory. The inset figure illustrates the linear fitting of the experimental data according to Eq. (1).

256 Fig. 8 shows the images of the field-emitted electrons taken
257 on the YAG screen at different solenoid currents, where the
258 SRF cavity gradient was 11.3 MV/m (corresponding to an
259 $E_{z,max}$ of 20 MV/m). When the solenoid field was increased
260 to 480 Gs, a clear focused spot could be observed, accom-
261 panied by a diffuse spot, as illustrated in Fig. 8(a). As the
262 solenoid field was increased to 640 Gs, the image evolved into
263 a clear ring. Note that the solenoid field of 640 Gs was close
264 to that required to focus the electron beam during typical op-
265 erations at a similar SRF cavity gradient; we can infer that
266 the ring-shaped electrons were emitted around the entrance
267 iris of the half cell of the SRF cavity. A comprehensive anal-
268 ysis of the images has been conducted in conjunction with
269 simulations, and the detailed findings will be presented later.

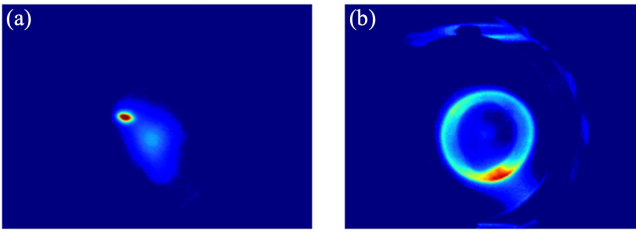


Fig. 8. The image of the field-emitted electrons on a YAG screen with a solenoid field of 480 Gs (a) and 640 Gs (b). The SRF gun was operated at an E_{acc} of 11.3 MV/m, corresponding to an $E_{z,max}$ of 20 MV/m.

270 Additional experimental efforts were undertaken to mea-
271 sure the energy spectrum of the field-emitted electrons using

272 a 90° dipole magnet located approximately 9 m downstream
273 from the photocathode. However, no dark current was de-
274 tected in front of the dipole, indicating that the field-emitted
275 electrons were largely scraped by the beam pipe during trans-
276 port.

IV. ANALYSIS AND DISCUSSION

A. Field-Emitted Electrons Tracking

279 Numerical simulations were conducted to analyze the dark
280 current with CST [40]. The CST Eigenmode Solver was first
281 utilized to simulate the three-dimensional RF field within the
282 SRF cavity. Particular attention was paid to the regions near
283 the cavity irises, where the mesh was locally refined to en-
284 hance the resolution of the RF field. The simulation uses
285 tetrahedral meshes with 80 cells per wavelength. Local re-
286 finement in the iris region is applied with a maximum step
287 size of 0.1 mm, and the total mesh count is 30 million. By
288 applying the magnetic boundary conditions, the final number
289 of mesh cells used for the simulation is 7.5 million. This en-
290 sured accurate field mapping in the regions susceptible to field
291 emission. The obtained RF field was then imported into the
292 Particle Tracking Solver for tracking field-emitted electrons.

293 In accordance with our experiments, the cavity gradient
294 E_{acc} was set to 11.3 MV/m. The tracking of the field-emitted
295 electrons from the SRF cavity surface was conducted along
296 a beam line with the same configuration as Fig. 5, and was
297 terminated at the position of the YAG screen located 1.5 m
298 downstream from the photocathode. The entrance irises of
299 the half cell and the full cell, where field emission is most
300 likely to occur, were individually designated as the electron
301 sources in the simulation. For both cases, the solenoid field
302 was set to 480 Gs and 640 Gs, respectively.

303 The initial electron energy was set to 4.3 eV, according to
304 the work function of niobium [41], and a 100% energy spread
305 was assumed to account for variations in emission energies.
306 The emission angles ranged from 0° to 90°, allowing for a
307 broad distribution of potential electron trajectories. Besides,
308 the surface secondary electron emission coefficient (SEC) for
309 niobium was incorporated from the CST database, providing
310 a more realistic depiction of emission behavior under the RF
311 fields.

312 We first tracked the electrons emitted from the entrance iris
313 of the half cell. The simulation showed that only electrons
314 emitted within the phase range of -105° to 45° were able to
315 transport to the beamline. When a proper solenoid field was
316 applied, a portion of the electrons could be focused at the
317 position of the YAG screen. Fig. 9 (a-b) and (c-d) illustrate
318 the spatial/transverse distributions of the electrons at solenoid
319 fields of 480 Gs and 640 Gs, respectively. The energy of the
320 electrons arriving at the YAG screen was between 1.82 MeV
321 and 1.98 MeV. When the solenoid field was 480 Gs, the lower
322 energy electrons were focused to a spot (see Fig. 9(a) and
323 (b)), similar to that in Fig. 8(a). As the solenoid field was in-
324 creased to 640 Gs, a large amount of higher energy electrons
325 converged, forming a ring (see Fig. 9(c) and (d)) with an in-

ner radius of 3.8 mm and an outer radius of 4.8 mm. This is similar to the dark current ring in Fig. 8(b), which has inner and outer radii of 3.6 mm and 4.7 mm, respectively.

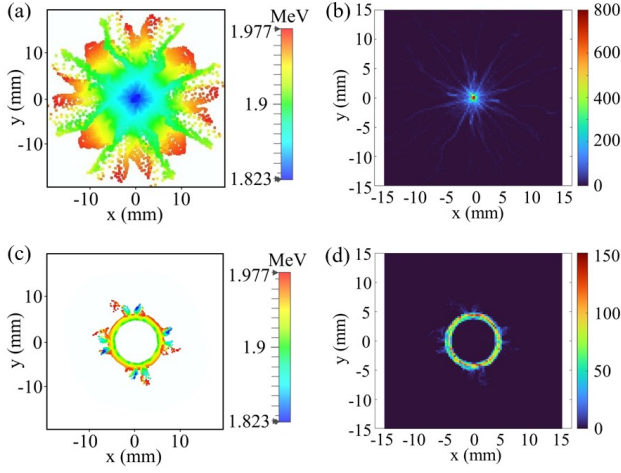


Fig. 9. Simulated distribution of the electrons emitted from the entrance iris of the half cell at 1.5 m downstream from the photocathode. (a) and (b) are the spatial energy and density distributions, respectively, at the solenoid strength of 480 Gs. **Electrons with an energy range of 1.8-1.9 MeV accumulate at the center of the screen, while electrons with higher energies (1.9-2.0 MeV) are dispersed at the outer edges of the beam;** (c) and (d) are the results at 640 Gs. **Electrons with the energy of 1.9-2.0 MeV form a ring-shaped pattern.** In the simulation, only a small fraction of particles were transported to the end, and the profiles did not exhibit perfect rotational symmetry.

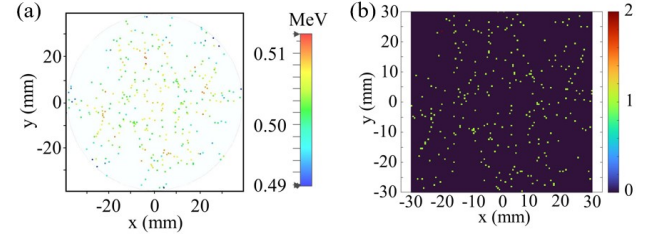


Fig. 10. Simulated distribution of the electrons emitted from the downstream side of the full-cell entrance iris at 1.5 m downstream from the photocathode. (a) and (b) are the spatial energy and density distributions, respectively. The solenoid strength is 480 Gs. **The field-emitted electrons have an energy of 0.5 MeV and are over-focused.**

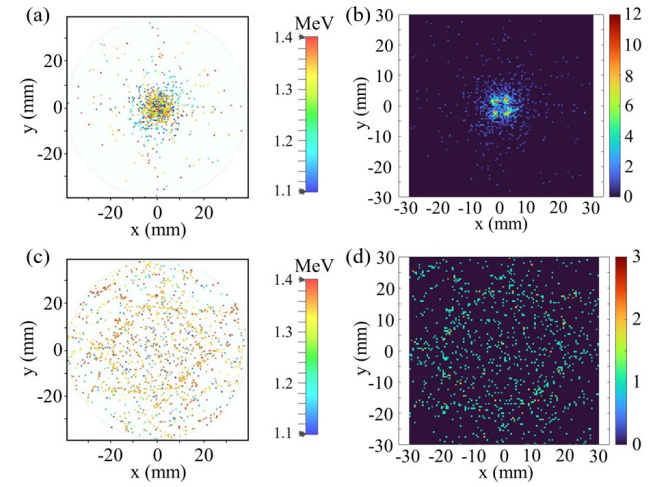


Fig. 11. Simulated distribution of the electrons emitted from the upstream side of the full-cell entrance iris at 1.5 m downstream from the photocathode. (a) and (b) are the spatial energy and density distributions, respectively, at the solenoid strength of 480 Gs; (c) and (d) are the results at 640 Gs. **The field-emitted electron energy is between 1.1 and 1.4 MeV.**

We then investigated the acceleration and transport of the electrons emitted from the downstream side of the full-cell entrance iris. In this case, higher energy electrons had large divergence angles due to stronger RF defocusing. **The electrons with energies higher than 0.8 MeV were scraped by the SRF cavity wall due to RF defocusing and cavity geometry, while those with energies between 0.52 and 0.8 MeV were scraped by the beam pipe.** Only a small amount of electrons with energy within the range of 0.45 to 0.52 MeV could transport to the position of the YAG screen. **Nevertheless, these electrons were over-focused at the solenoid field of 480 Gs (see Fig. 10).** This suggests that field-emitted electrons from the downstream side of the full-cavity entrance iris are not the source of the diffuse spots observed in Fig. 8(a).

We finally tracked the electrons emitted from the upstream side of the full-cell entrance iris, where the maximum surface field occurred as indicated in Fig. 3(b). The simulation indicated that only electrons emitted at the phase between 200° and 220° had the chance to arrive at the beam line. These electrons initially moved upstream toward the back wall of the half cell, and the velocity decreased to zero. Then the electrons underwent acceleration and moved downstream, reaching energies between 1.1 to 1.4 MeV at the SRF cavity exit. At a solenoid field of 480 Gs, a portion of the electrons can be focused to an area with a radius of 4 mm, as illustrated in Fig. 11(a) and (b). This may align with the diffuse spot observed in Fig. 8(a). When the solenoid field was increased to 640

Gs, the electrons became over-focused and subsequently dispersed, as shown in Fig. 11(c) and (d). This can explain why we could only observe the ring-shaped profile in Fig. 8(b) at 640 Gs.

To sum up, the dark current observed in the experiment can be attributed to two distinct sources: the entrance iris of the half cell (referred to as "A") and the upstream side of the full-cell entrance iris (referred to as "B"). At the solenoid field of 480 Gs, the lower energy portion (~ 1.8 MeV) of the electrons emitted from A were focused and formed the bright spot in Fig. 8(a), while the electrons ($1.1 \sim 1.4$ MeV) emitted from B were focused and formed the diffuse spot in the figure. At the solenoid field of 640 Gs, the higher energy portion (~ 1.9 MeV and above) of the electrons from A were focused and formed the ring in Fig. 8(b), which depicts the shape of the half-cell entrance iris of the SRF cavity. The electrons from B, however, became over-focused and dispersed. Note the displacement of the centers of the two spots in Fig. 8(a),

which owes to the misalignment of the solenoid with the SRF cavity.

B. Experimental Data Fitting

According to Fowler-Nordheim (F-N) theory[42], the dark current due to field emission from the SRF cavity can be evaluated as

$$\frac{d\left(\log_{10}\left(\frac{\bar{I}_F}{E_{acc}^{2.5}}\right)\right)}{d\left(\frac{1}{E_{acc}}\right)} = -\frac{2.84 \times 10^3 \Phi^{1.5}}{\kappa \beta} \quad (1)$$

where \bar{I}_F is the average field emission current over one radiofrequency cycle (in nA), the cavity gradient E_{acc} is in MV/m, Φ is the work function of the emitting material (in eV, and 4.3 herein for Nb), κ represents the ratio between surface electric field and the cavity gradient, while β is the field enhancement factor due to the aspect ratio of local geometry and is susceptible to microscopic surface defects such as scratches, protrusions, and particles. By conducting a linear fitting of the equation, the field enhancement factor can be determined and subsequently utilized to evaluate the surface condition of the SRF cavity. Note that in the equation E_{acc} is used instead of the surface electric field. Subsequently, the parameter κ is introduced to account for the transformation. Given that the measured dark current **primarily** originated from the field emission around the entrance iris of the half cell, κ is set to 1.65, representing the ratio between peak electric field within this region and E_{acc} .

TABLE 2. Key parameters in Equation (1)

Parameter	Value	Unit
Φ	4.3	eV
κ	1.65	-

The fitting for the dark current measurements of the SRF cavity in Sec. 3.3 is illustrated in Fig. 7. For comparison, we also included the result for an earlier measurement where the SRF cavity had been exposed to air accidentally for a few times, leading to a poor surface condition. As a result, the cavity only operated at a gradient below 12 MV/m due to concerns about radiation induced by field-emitted electrons. The measured dark current at such a gradient was 44.5 pA (10%

duty cycle). To improve performance, the DC-SRF gun was disassembled and underwent HPR. After reassembly, the operational gradient of the cavity was increased to 14.8 MV/m as mentioned earlier. The field enhancement factors obtained from the fit are 291 before HPR and 227 after HPR, indicating a significant improvement in the surface condition of the SRF cavity. It is worth mentioning that the correlation coefficients for the F-N linear fitting are 0.998 and 0.997 in the two cases, respectively. The good agreement between the measured data sets and Eq. (1) indicates the validity of the theoretical model, which assumes the measured dark current is mostly emitted from the entrance iris of the half cell. Also note that the measured dark current is only a part of the electrons emitted from the cavity surface. The field emission in the SRF cavity would be higher, as indicated by the simulations.

V. SUMMARY

In summary, we have presented both the experimental and simulation study on the dark current from the high-brightness DC-SRF photocathode gun. Benefit from the design, the conditioning of the DC electrodes and SRF cavity has effectively eliminated the field emitters, enabling the DC-SRF gun to operate at the designed DC voltage and SRF cavity gradient. This has laid a solid foundation for the high-performance operation of the DC-SRF-II gun. In particular, CW operation with a dark current several orders lower than current normal conducting CW guns has been achieved. Our experiments and simulations are in good agreement, showing that the dark current during operation **primarily** originates from field emission at the entrance iris of the SRF cavity. These electrons exhibit a ring-shaped distribution and can be effectively eliminated using an aperture in the beam line. **Additionally, careful processing of the SRF cavity (including HPR) and improving the cleanliness of the assembly environment could further decrease the dark current, so as to obtain a very clean high-brightness electron beam for various applications.**

ACKNOWLEDGMENTS

The authors would like to show their gratitude to J.Hao, H.Xu, F.Wang, F.Zhu, X.Zhang, M.Ren, Z.Yao, Z.Wang and D.Wang for very helpful discussions.

- [1] P. Emma, R. Akre, J. Arthur et al., First lasing and operation of an Ångström-wavelength free-electron laser, *Nature Photonics*, **4**, 641–647 (2010). doi:10.1038/nphoton.2010.176
- [2] C. Bostedt, S. Boutet, D.M. Fritz et al., Linac Coherent Light Source: The first five years, *Rev. Mod. Phys.*, **88**, 015007 (2016). doi:10.1103/RevModPhys.88.015007
- [3] C. Feng, H.-X. Deng et al., Review of fully coherent free-electron lasers, *Nuclear Science and Techniques*, **29**, 160

- (2018). doi:10.1007/s41365-020-0732-x
- [4] W. Decking, S. Abeghyan, P. Abramian et al., A MHz-repetition-rate hard X-ray free-electron laser driven by a superconducting linear accelerator, *Nature Photonics*, **14**, 391–397 (2020). doi:10.1038/s41566-020-0607-z
- [5] E. Prat, R. Abela, M. Aiba et al., A compact and cost-effective hard X-ray free-electron laser driven by a high-brightness and low-energy electron beam, *Nature Photonics*, **14**, 748–754

- (2020). doi:10.1038/s41566-020-00712-8
- [6] J.-D. Fan, Y.-J. Tong, Y.-G. Nie et al., First commissioning results of the coherent scattering and imaging endstation at the Shanghai soft X-ray free-electron laser facility, *Nuclear Science and Techniques*, **33**, 114 (2022). doi:10.1007/s41365-022-0146-1
- [7] G.R. Neil, C. Behre, S.V. Benson et al., The JLab high power ERL light source, *Nuclear Instruments and Methods in Physics Research Section A: Accelerators, Spectrometers, Detectors and Associated Equipment*, **557**, 9–15 (2006). doi:10.1016/j.nima.2006.01.122
- [8] A. Hutton et al., Energy-recovery linacs for energy-efficient particle acceleration, *Nature Reviews Physics*, **5**, 708–716 (2023). doi:10.1038/s41586-022-04678-1
- [9] A. Bartnik, N. Banerjee, D. Burke et al., CBETA: first multipass superconducting linear accelerator with energy recovery, *Physical Review Letters*, **125**, 044803 (2020). doi:10.1103/PhysRevLett.125.044803
- [10] J. Wu, M. Tang, L. Zhao et al., Ultrafast atomic view of laser-induced melting and breathing motion of metallic liquid clusters with MeV ultrafast electron diffraction, *Proceedings of the National Academy of Sciences*, **119**, e2111949119 (2022). doi:10.1073/pnas.2111949119
- [11] S.P. Weathersby, G. Brown, M. Centurion et al., Mega-electron-volt ultrafast electron diffraction at SLAC National Accelerator Laboratory, *Review of Scientific Instruments*, **86**, 7 (2015). doi:10.1063/1.4929430
- [12] L.W. Feng, L. Lin, S.L. Huang et al., Ultrafast electron diffraction with megahertz MeV electron pulses from a superconducting radio-frequency photoinjector, *Applied Physics Letters*, **107**, 22 (2015). doi:10.1063/1.4937199
- [13] J.H. Han, M. Krasilnikov, K. Flöttmann et al., Secondary electron emission in a photocathode rf gun, *Physical Review Special Topics—Accelerators and Beams*, **8**, 3 (2005). doi:10.1103/PhysRevSTAB.8.033501
- [14] D.H. Dowell, E. Jongewaard, C. Limborg-Deprey et al., Measurement and analysis of field emission electrons in the LCLS gun, in *Proceedings of the 2007 IEEE Particle Accelerator Conference (PAC)*, pp. 1299–1301 (2007). doi:10.1109/PAC.2007.4440702
- [15] L. Frohlich, Dark current transport in the FLASH linac, in *Proceedings of the 2007 IEEE Particle Accelerator Conference (PAC)*, pp. 956–958 (2007). doi:10.1109/PAC.2007.4440757
- [16] D. Lipka, W. Kleen, J. Lund-Nielsen et al., Dark current monitor for the European XFEL, in *Proceedings of DIPAC* (2011). doi:10.18429/JACoW-DIPAC2011-MOPD49
- [17] H. Chen, Y. Du, W. Gai et al., Surface-Emission Studies in a High-Field RF Gun based on Measurements of Field Emission and Schottky-Enabled Photoemission, *Physical Review Letters*, **109**, 20 (2012). doi:10.1103/PhysRevLett.109.204802
- [18] J. Teichert, A. Arnold, P. Murcek et al., Dark Current in Superconducting RF Photoinjectors—Measurements and Mitigation, in *Proceedings of the 53rd ICFA Advanced Beam Dynamics Workshop on Energy Recovery Linacs (ERL2013)*, pp. 75–79 (2013).
- [19] C. Gulliford, A. Bartnik, I. Bazarov et al., Demonstration of low emittance in the Cornell energy recovery linac injector prototype, *Phys. Rev. ST Accel. Beams*, **16**, 073401 (2013). doi:10.1103/PhysRevSTAB.16.073401
- [20] R. Xiang, A. Arnold, T. Kamps et al., Experimental studies of dark current in a superconducting rf photoinjector, *Physical Review Special Topics—Accelerators and Beams*, **17**, 4 (2014). doi:10.1103/PhysRevSTAB.17.043401
- [21] A. Bartnik, C. Gulliford, I. Bazarov et al., Operational experience with nanocoulomb bunch charges in the Cornell photoinjector, *Phys. Rev. ST Accel. Beams*, **18**, 083401 (2015). doi:10.1103/PhysRevSTAB.18.083401
- [22] R. Huang, D. Filippetto, C.F. Papadopoulos et al., Dark current studies on a normal-conducting high-brightness very-high-frequency electron gun operating in continuous wave mode, *Physical Review Special Topics—Accelerators and Beams*, **18**, 013401 (2015). doi:10.1103/PhysRevSTAB.18.013401
- [23] J. Shao, J. Shi, S.P. Antipov et al., In situ observation of dark current emission in a high gradient rf photocathode gun, *Physical Review Letters*, **117**, 084801 (2016). doi:10.1103/PhysRevLett.117.084801
- [24] H. Xu, M.A. Shapiro, R.J. Temkin et al., Measurement of internal dark current in a 17 GHz, high gradient accelerator structure, *Physical Review Accelerators and Beams*, **22**, 021002 (2019). doi:10.1103/PhysRevAccelBeams.22.021002
- [25] N. Nishimori, R. Nagai, R. Hajima et al., Operational experience of a 500 kV photoemission gun, *Phys. Rev. Accel. Beams*, **22**, 053402 (2019). doi:10.1103/PhysRevAccelBeams.22.053402
- [26] I. Petrushina, V.N. Litvinenko, Y. Jing et al., High-Brightness Continuous-Wave Electron Beams from Superconducting Radio-Frequency Photoemission Gun, *Phys. Rev. Lett.*, **124**, 244801 (2020). doi:10.1103/PhysRevLett.124.244801
- [27] F. Zhou, C. Adolphsen, A. Benwell et al., Commissioning of the SLAC Linac Coherent Light Source II electron source, *Phys. Rev. Accel. Beams*, **24**, 073401 (2021). doi:10.1103/PhysRevAccelBeams.24.073401
- [28] G. Shu, H. Qian, N. Aftab et al., Dark current studies of an L-band normal conducting RF gun, *Nuclear Instruments and Methods in Physics Research Section A: Accelerators, Spectrometers, Detectors and Associated Equipment*, **1010**, 165546 (2021). doi:10.1016/j.nima.2021.165546
- [29] F. Qiu, Y. He, A.D. Wu et al., In situ mitigation strategies for field emission-induced cavity faults using low-level radiofrequency system, *Nuclear Science and Techniques*, **33**, 140 (2022). doi:10.1007/s41365-022-0146-1
- [30] F. Zhou, C. Adolphsen, D. Dowell et al., Overview of CW electron guns and LCLS-II RF gun performance, *Frontiers in Physics*, **11**, (2023). doi:10.3389/fphy.2023.1150809
- [31] R. Xiang, A. Arnold, J.W. Lewellen et al., Superconducting radio frequency photoinjectors for CW-XFEL, *Frontiers in Physics*, **11**, (2023). doi:10.3389/fphy.2023.1166179
- [32] L. Zheng, H. Chen, B. Gao et al., Design, fabrication, and beam commissioning of a 216.667 MHz continuous-wave photocathode very-high-frequency electron gun, *Phys. Rev. Accel. Beams*, **26**, 103402 (2023). doi:10.1103/PhysRevAccelBeams.26.103402
- [33] X.-H. Wang, G. Shu, H. Qian et al., Experimental demonstration of dark current mitigation by an over-inserted plug in a normal conducting VHF gun, *arXiv preprint arXiv:2411.01754*, (2024). arXiv:2411.01754
- [34] K. Zhao, J. Hao, Y. Hu et al., Research on DC-RF superconducting photocathode injector for high average power FELs, *Nuclear Instruments and Methods in Physics Research Section A: Accelerators, Spectrometers, Detectors and Associated Equipment*, **475**, 564–568 (2001). doi:10.1016/S0168-9002(01)00498-9
- [35] R. Xiang, Y. Ding, K. Zhao et al., Experimental investigations of DC-SC photoinjector at Peking University, *Nuclear Instruments and Methods in Physics Research Section A: Accelerators, Spectrometers, Detectors and Associated Equipment*, **528**,

- 321–325 (2004). doi:[10.1016/j.nima.2004.03.068](https://doi.org/10.1016/j.nima.2004.03.068)
- [36] J. Hao, X. Lu, Y. Ding et al., Primary beam-loading tests on DC–SC photoinjector at Peking University, *Nuclear Instruments and Methods in Physics Research Section A: Accelerators, Spectrometers, Detectors and Associated Equipment*, **557**, 138–141 (2006). doi:[10.1016/j.nima.2006.01.086](https://doi.org/10.1016/j.nima.2006.01.086)
- [37] S. Quan, F. Zhu, J. Hao et al., 3.5-cell large grain niobium superconducting cavity for a DC superconducting RF photoinjector, *Physical Review Special Topics—Accelerators and Beams*, **13**, 042001 (2010). doi:[10.1103/PhysRevSTAB.13.042001](https://doi.org/10.1103/PhysRevSTAB.13.042001)
- [38] S. Quan, J. Hao, L. Lin et al., Stable operation of the DC-SRF photoinjector, *Nucl. Instrum. Methods Phys. Res., Sect. A*, **798**, 117–120 (2015). doi:[10.1016/j.nima.2015.07.025](https://doi.org/10.1016/j.nima.2015.07.025)
- [39] H. Jia, T. Li, T. Wang et al., High-brightness megahertz-rate beam from a direct-current and superconducting radio-frequency combined photocathode gun, *Phys. Rev. Res.*, **6**, 043165 (2024). doi:[10.1103/PhysRevResearch.6.043165](https://doi.org/10.1103/PhysRevResearch.6.043165)
- [40] CST Studio Suite 2020, <http://www.cst.com>, 2020.
- [41] P.V. Tyagi, M. Doleans, B. Hannah et al., Improving the work function of the niobium surface of SRF cavities by plasma processing, *Applied Surface Science*, **369**, 29–35 (2016). doi:[10.1016/j.apsusc.2016.01.089](https://doi.org/10.1016/j.apsusc.2016.01.089)
- [42] J.W. Wang, G.A. Loew, Report No. SLAC-PUB-7684, Stanford Linear Accelerator Center, Menlo Park, CA (USA), (1997).